

Data-Driven Turbulence Modeling Approach for Cold-Wall Hypersonic Boundary Layers

Muhammad I. Zafar^{*}, Xuhui Zhou[†], and Christopher J. Roy[‡]
Virginia Polytechnic Institute and State University, Blacksburg, Virginia 24061

David Stelter[§]
Spectral Sciences Inc., Burlington, Massachusetts 01803

Heng Xiao[¶]
University of Stuttgart, Stuttgart, Germany

Wall-cooling effect in hypersonic boundary layers can significantly alter the near-wall turbulence behavior, which is not accurately modeled by traditional RANS turbulence models. To address this shortcoming, this paper presents a turbulence modeling approach for hypersonic flows with cold-wall conditions using an iterative ensemble Kalman method. Specifically, a neural-network-based turbulence model is used to provide closure mapping from mean flow quantities to Reynolds stress as well as a variable turbulent Prandtl number. Sparse observation data of velocity and temperature are used to train the turbulence model. This approach is analyzed using direct numerical simulation database for boundary layer flows over a flat plate with a Mach number between 6 and 14 and wall-to-recovery temperature ratios ranging from 0.18 to 0.76. Two training cases are conducted: 1) a single training case with observation data from one flow case, 2) a joint training case where data from two flow cases are simultaneously used for training. Trained models are also tested for generalizability on the remaining flow cases in each of the training cases. The results are also analyzed for insights to inform the future work towards enhancing the generalizability of the learned turbulence model.

Nomenclature

- \mathbf{a} = deviatoric part of the Reynolds stress tensor, Pa
 C_f = $\tau_w / (\frac{1}{2} \rho_\infty U_\infty^2)$; wall skin friction coefficient
 $C_{h,aw}$ = $q_w / (\rho_\infty c_p U_\infty (T_r - T_w))$; wall heat transfer coefficient
 $C_{h,e}$ = $q_w / (\rho_\infty c_p U_\infty (T_{0,e} - T_w))$; wall heat transfer coefficient

^{*}Ph.D. Student, Aerospace and Ocean Engineering.

[†]Ph.D. Student, Aerospace and Ocean Engineering.

[‡]Professor, Aerospace and Ocean Engineering. Associate Fellow AIAA.

[§]Group Leader, Machine Learning and Data Analytics.

[¶]Professor, Stuttgart Center for Simulation Science (SimTech)

c_p	=	heat capacity at constant pressure, J/(K.kg)
E	=	total energy, J
f	=	generic solution variable
F_s	=	factor of safety
$g^{(n)}$	=	scalar coefficient of n -th tensor basis
H	=	total enthalpy, J
J	=	cost function
K	=	Kalman gain matrix
k	=	turbulent kinetic energy, J/kg
k_T	=	thermal conductivity, W/(m·K)
M	=	Mach number
P	=	model error covariance matrix
p	=	pressure, Pa
Pr	=	0.71; molecular Prandtl number
Pr_t	=	turbulent Prandtl number
q_j	=	local heat flux component in x_j direction, W/m ²
q_w	=	wall heat flux, W/m ²
R	=	observation error covariance matrix
Re_τ	=	$\rho_w u_\tau \delta / \mu_w$; Reynolds number based on friction velocity and wall viscosity
\mathbf{S}	=	$\frac{1}{2} \left(\frac{\partial u_i}{\partial x_j} + \frac{\partial u_j}{\partial x_i} \right)$; strain rate tensor (also represented as S_{ij}), s ⁻¹
T	=	temperature, K
$\mathbf{T}^{(n)}$	=	n -th tensor basis
t	=	time, s
t_s	=	turbulent time scale, s
T_r	=	$(1 + 0.89(\gamma - 1)M_\infty^2) T_\infty$; recovery temperature, K
$T_{0,e}$	=	$T_e + \frac{1}{2c_p} U_e^2$; total temperature at the boundary layer edge, K
Tu	=	$100 \sqrt{\frac{2}{3} \frac{k_\infty}{U_\infty^2}}$; turbulent intensity
U_∞	=	freestream velocity, m/s
u	=	streamwise velocity component, m/s
u_j	=	velocity in x_j direction, m/s
u_{VD}^+	=	$\frac{1}{u_\tau} \int_0^{\bar{u}} (\bar{\rho} / \bar{\rho}_w)^{1/2} d\bar{u}$, Van Driest transformed mean velocity
u_τ	=	$\sqrt{\tau_w / \rho_w}$; friction velocity, m/s

x	=	streamwise direction, m
x_a	=	streamwise location of sampling wall-normal profiles, m
x_i	=	streamwise location where δ matches inflow boundary-layer thickness of direct numerical simulation data, m
Y	=	observation data
y	=	wall-normal direction, m
y^+	=	$y\rho_w u_\tau / \mu_w$, non-dimensional distance in wall-normal direction
δ	=	boundary-layer thickness (based on 99% of the freestream velocity), m
δ_i	=	boundary-layer thickness at inflow plane of direct numerical simulation data, mm
ϵ_h	=	discretization error
γ	=	c_p/c_v , specific heat ratio
\mathcal{H}	=	model operator
μ	=	dynamic viscosity, kg/(m·s)
μ_t	=	eddy viscosity, kg/(m·s)
ρ	=	density, kg/m ³
σ_{ij}	=	viscous stress tensor, Pa
τ	=	Reynolds stress tensor (also represented as τ_{ij}), Pa
τ_w	=	wall shear stress, Pa
ω	=	turbulent specific dissipation, s ⁻¹
Ω	=	$\frac{1}{2} \left(\frac{\partial u_i}{\partial x_j} - \frac{\partial u_j}{\partial x_i} \right)$; rotation rate tensor (also represented as Ω_{ij}), s ⁻¹
θ	=	scalar invariants
w	=	neural network parameters

Subscripts

aw	=	adiabatic wall value
e	=	edge condition
∞	=	freestream quantity
w	=	wall variable

Superscripts

l	=	iteration index during model training
$+$	=	variable in inner wall units

I. Introduction

TURBULENCE modeling is arguably the most crucial aspect of high Reynolds number hypersonic flow computations. Hypersonic flight conditions are characterized by extremely high kinetic energy in the flow, which dissipates as heat energy near the surface of the vehicle. The heating rates in the turbulent boundary layer can be several times higher than the laminar boundary layer. Furthermore, as a result of radiative cooling and internal heat transfer, the external surface temperatures of hypersonic flight vehicles are often considerably lower than the adiabatic wall temperature. These cold wall conditions result in substantial thermal gradients between the surface and the fluid, which in turn modify the characteristics of near-wall turbulence. Similar cold wall conditions can also arise in wind tunnel experiments, where the short duration of the experiments prevents the test article from reaching higher temperatures. Therefore, the accurate modeling of cold-wall hypersonic turbulent boundary layers is of utmost importance for predicting surface heat flux and ensuring reliable thermal protection design for such vehicles.

The most commonly used turbulence models in Reynolds-averaged Navier-Stokes (RANS) simulations are typically calibrated for incompressible flow conditions. Extensive validation has been conducted for subsonic or moderately supersonic flows, where significant near-wall heat flux is absent. According to the Morkovin hypothesis [1], when variations in mean thermodynamic quantities are appropriately accounted for, incompressible turbulence models have demonstrated satisfactory performance in capturing mean velocity and mean temperature fields in compressible turbulent boundary layers. So et al. [2] further established that the Morkovin hypothesis extends to turbulence quantities, indicating a dynamic similarity between the near-wall turbulence characteristics of incompressible and compressible wall-bounded turbulent flows. However, the validity of this hypothesis diminishes as the Mach number increases into the hypersonic regime, and these turbulence models exhibit progressively poorer performance, particularly in cold-wall scenarios [3]. To address these limitations, several compressibility corrections have been proposed. A comprehensive review and evaluation of turbulence models for hypersonic flows can be found in Ref. [4]. Compressibility corrections for hypersonic boundary layer applications have also been analyzed in Ref. [3] that emphasizes the existing need for improved turbulence models specifically tailored for hypersonic flows.

In cold-wall cases, direct numerical simulations (DNS) have revealed that the effect of wall cooling can significantly alter the near-wall turbulence structure [5], which is not adequately accounted for by RANS models. At hypersonic flow conditions, RANS turbulence models have been shown to overestimate wall heat transfer and skin-friction by up to 30% [6] when compared to DNS data [7, 8]. Moreover, as the wall cooling effect and freestream Mach number increase, RANS models tend to overestimate the peak temperature in the boundary layer by nearly 25% [6]. In an effort to address these issues, a compressibility correction was proposed and analyzed for the $k-\omega$ model in cold-wall hypersonic flow cases [9]. This compressibility correction demonstrated improvements in velocity and skin-friction estimation. However, its impact on the computation of boundary layer peak temperature and heat transfer was minimal. The proposed compressibility correction primarily focuses on enhancing the prediction of eddy viscosity to improve the

estimation of wall heat flux as a second-order effect.

One notable source of uncertainty in turbulence modeling, particularly for hypersonic flows, is the assumption of a constant turbulent Prandtl number throughout the boundary layer and across different Mach numbers. This assumption has been identified as a source of uncertainty in various studies, particularly those related to hypersonic flows [3, 6]. Researchers have addressed this problem by introducing a variable turbulent Prandtl number formulation based on a two-equation model for enthalpy variance and its dissipation rate [10]. They demonstrated improvements in heat transfer prediction for flows involving separated regions and shock–wave/boundary-layer interactions. Therefore, there is a strong case for incorporating a modeling approach that considers variable turbulent Prandtl number along with Reynolds Stresses in the development of turbulence models specifically tailored for hypersonic flows.

In the domain of data–driven turbulence modeling [11], machine learning methods have been predominantly employed over the past decade to systematically utilize data for the development of more robust and generalizable turbulence models [12–15]. Typically, these machine learning models have been trained using *direct data* of closure terms (i.e. Reynolds stresses) obtained from high–fidelity simulations (e.g., DNS). However, the availability of such high–fidelity data is primarily limited to simple geometries or low Reynolds numbers. Furthermore, when trained turbulence models are coupled with RANS solvers, they often yield poor predictions of mean flow quantities [16]. This discrepancy arises due to inconsistencies between the training and prediction environments [17]. Therefore, it is desirable to utilize *indirect data*, which encompasses quantities like velocity, temperature, lift coefficients, etc., within a model–consistent learning framework [17] that involves the RANS solvers in the training process. Numerous approaches have been proposed in this regard, including adjoint-based methods [18, 19], ensemble-based learning [20], symbolic regression [21], and the ensemble Kalman method [22]. In terms of directly modeling turbulent heat flux closure, a model–consistent approach based on gene-expression programming (GEP) has been employed to learn varying turbulent Prandtl number for an incompressible flow case, although the eddy viscosity term was not modeled in this approach [23].

In this work, a neural–network–based turbulence model for hypersonic boundary layer flow over a cold wall is developed, using a model–consistent framework based on iterative ensemble Kalman method. Specifically, a linear eddy viscosity model along with a variable turbulent Prandtl number is learned to enhance the accuracy of wall heat flux predictions. Sparse observation data of velocity and temperature are used for the training. To train the neural network (NN), the iterative ensemble Kalman method is employed, which has demonstrated superior efficiency and accuracy compared to other model–consistent training frameworks. Unlike the gradient-free GEP method, the ensemble Kalman method approximates the gradient and Hessian based on the statistics of the ensemble of simulation results, resulting in improved efficiency. Furthermore, in contrast to adjoint-based methods, the ensemble Kalman method requires significantly less implementation effort due to its non-intrusive nature.

This paper represents an initial step in the development of data–driven turbulence models for hypersonic flows, aiming to encompass a wider range of flow conditions. To this end, the observation data utilized here for training is

obtained from a recent DNS database for hypersonic boundary layer flows over a flat plate with zero–pressure gradient (ZPG). The database includes various flow cases with wall–to–recovery temperature ratios (T_w/T_r) ranging from 0.18 to 0.76 and Mach numbers between 6 and 14. The remainder of the paper is organized as follows. § II introduces the representation of closure terms for compressible flows and provides an overview of the employed training framework. § III presents and analyzes benchmark hypersonic flow cases, along with the corresponding grids generated for the respective RANS simulations. § IV presents and discusses the training and testing results. Finally, § V concludes the paper.

II. Methodology

For compressible flows, the Favre–averaged equations for conservation of mass, momentum, and energy can be written as:

$$\frac{\partial \bar{\rho}}{\partial t} + \frac{\partial}{\partial x_j} (\bar{\rho} \hat{u}_j) = 0 \quad (1a)$$

$$\frac{\partial (\bar{\rho} \hat{u}_i)}{\partial t} + \frac{\partial}{\partial x_j} (\hat{u}_j \bar{\rho} \hat{u}_i) = -\frac{\partial p}{\partial x_i} + \frac{\partial \bar{\sigma}_{ij}}{\partial x_j} + \frac{\partial \tau_{ij}}{\partial x_j} \quad (1b)$$

$$\frac{\partial (\bar{\rho} \hat{E})}{\partial t} + \frac{\partial}{\partial x_j} (\hat{u}_j \bar{\rho} \hat{H}) = \frac{\partial (\bar{\sigma}_{ij} \hat{u}_i)}{\partial x_j} + \frac{\partial (\hat{u}_i \tau_{ij})}{\partial x_j} - \frac{\partial (\bar{q}_j)}{\partial x_j} - \frac{\partial (c_p \overline{\rho u_j'' T''})}{\partial x_j} \quad (1c)$$

where the hat sign ($\hat{\cdot}$) over a variable represents the Favre–average (density–weighted) quantity and the overbar ($\bar{\cdot}$) denotes Reynolds–averaged quantity. The viscous stress tensor (σ_{ij}) and laminar heat flux (q_j) are described as:

$$\bar{\sigma}_{ij} \approx 2\hat{\mu} \left(\hat{S}_{ij} - \frac{1}{3} \frac{\partial \hat{u}_k}{\partial x_k} \delta_{ij} \right), \quad \bar{q}_j = -\overline{k_T \partial T / \partial x_j} \approx -\frac{c_p \hat{\mu}}{Pr} \frac{\partial \hat{T}}{\partial x_j}$$

where thermal conductivity (k_T) is approximated using dynamic viscosity (μ) and Prandtl number (Pr). In the above Favre–averaged equations (Eq. 1), the Reynolds stress (τ_{ij}) and turbulent heat flux ($q_j^{(t)} = c_p \overline{\rho u_j'' T''}$) terms need to be modeled.

A. Modeling of closure terms

Reynolds stress term ($\tau = \tau_{ij}$) can be decomposed into a deviatoric part (**a**) and a spherical (or dilatational) part, as:

$$\tau = \mathbf{a} - \frac{2}{3} \bar{\rho} k \mathbf{I} \quad (2)$$

Based on the general effective–viscosity model [24], the Reynolds stresses can be formulated as a function of only the normalized strain rate tensor $\hat{\mathbf{S}} (= t_s \mathbf{S})$ and the rotation rate tensor $\hat{\mathbf{\Omega}} (= t_s \mathbf{\Omega})$, where $t_s = 1/(\beta^* \omega)$ represents the turbulent timescale [25]. Here, β^* is a model constant, and the specific turbulence dissipation rate (ω) is obtained by

solving the respective transport equation given by the k - ω turbulence model.

The most general form of \mathbf{a} can be expressed as a linear combination of isotropic basis tensors. (\mathbf{T}):

$$\mathbf{a} = 2\bar{\rho}k \sum_{n=1}^{10} g^{(n)} \mathbf{T}^{(n)} \quad (3)$$

where scalar coefficients $g^{(n)}$ may be functions of independent invariants of $\hat{\mathbf{S}}$ and $\hat{\mathbf{\Omega}}$ [24]. Owing to the Cayley–Hamilton theorem, there is only a finite number of independent basis tensors and invariants that can be formed from $\hat{\mathbf{S}}$ and $\hat{\mathbf{\Omega}}$. Detailed derivation of these independent basis tensors can be found in Ref.[24], and the linear and quadratic basis tensors are listed here:

$$\mathbf{T}^{(1)} = \hat{\mathbf{S}} - \frac{1}{3}\{\hat{\mathbf{S}}\}, \quad \mathbf{T}^{(2)} = \hat{\mathbf{S}}\hat{\mathbf{\Omega}} - \hat{\mathbf{\Omega}}\hat{\mathbf{S}}, \quad \mathbf{T}^{(3)} = \hat{\mathbf{S}}^2 - \frac{1}{3}\{\hat{\mathbf{S}}^2\}, \quad \mathbf{T}^{(4)} = \hat{\mathbf{\Omega}}^2 - \frac{1}{3}\{\hat{\mathbf{\Omega}}^2\}$$

where the curly bracket $\{\cdot\}$ denotes the trace of the matrix.

The functional basis of invariants has been derived in Ref.[26], which can be used for the functional representation of scalar coefficients: $\theta \mapsto \mathbf{g}$. Using these invariants as input features embeds the Galilean invariance in the model representation. For two-dimensional compressible flows, there are only three non-zero independent invariants[24, 27]:

$$\theta_1 = \{\hat{\mathbf{S}}\}, \quad \theta_2 = \{\hat{\mathbf{S}}^2\}, \quad \theta_3 = \{\hat{\mathbf{\Omega}}^2\} \quad (4)$$

In the case of compressible flows, the consideration of a non-zero trace of the strain rate is necessary [27], leading to the first invariant.

For this work, we consider only linear representation of deviatoric Reynolds stress, akin to linear eddy viscosity model following the Boussinesq hypothesis [28]. Consequently, the turbulent eddy viscosity (μ_t) is estimated using the first term of the integrity basis representation as:

$$\mu_t = -\frac{g^{(1)}\rho k}{\beta^*\omega} \quad (5)$$

where $g^{(1)}$ is the scalar coefficient of the first tensor basis.

Second closure term is the turbulence heat flux ($q_j^{(t)}$), for which Reynolds analogy is most commonly used to model the term as:

$$q_j^{(t)} = c_p \overline{\rho u_j'' T''} \approx -\frac{c_p \mu_t}{Pr_t} \frac{\partial \hat{T}}{\partial x_j} \quad (6)$$

where the turbulent Prandtl number (Pr_t) is typically assumed having a constant value. However, in this work, we address the uncertainty associated with this constant value assumption by learning a variable Pr_t .

Based on the aforementioned representations of the closure terms for Reynolds stress and turbulent heat flux, the closure modeling involves the learning of a scalar coefficient $g^{(1)}$ and a variable Pr_t . To accomplish this, a neural network is employed to predict these two quantities as functions of scalar invariants (θ_1, θ_2 and θ_3). The subsequent section elaborates on the framework for model-consistent training of this NN-based closure model.

B. Ensemble Kalman method for training

To learn the NN-based closure model, we employ the ensemble Kalman method to infer the parameters \mathbf{w} of this neural network. The ensemble Kalman method is a data assimilation technique that finds application in a diverse range of fields and disciplines [22, 29–31]. It effectively combines the information from an ensemble of model simulations and the available observational data to provide a statistical inference of the system's state. In the current research work, the system's state corresponds to the parameters \mathbf{w} of the NN-based closure model. For the iterative process of training these parameters, the corresponding cost function is formulated as:

$$J = \|\mathbf{w}^{l+1} - \mathbf{w}^l\|_P + \|Y - \mathcal{H}[\mathbf{w}^{l+1}]\|_R \quad (7)$$

where l is the iteration index, and $\|\cdot\|$ represents the norm weighted by the matrices P and R for the respective terms. P represents the model error covariance matrix, reflecting the uncertainties associated with the model parameters, while R denotes the observation error covariance matrix for the observation data Y . During each iteration, the parameters \mathbf{w} are mapped to quantities in observation space (e.g., velocity and temperature) by the operator \mathcal{H} . Hence, \mathcal{H} denotes the process of predicting closure variables, forward propagation of RANS equations and post-processing, and the term $\mathcal{H}[\mathbf{w}]$ represents the predicted observed quantities.

The first term in Eq. 7 provides regularization for the updated parameters \mathbf{w} by penalizing large changes, while the second term penalizes the difference between the observational data Y and the model prediction $\mathcal{H}[\mathbf{w}]$.

In the ensemble Kalman method, the update scheme for the parameters \mathbf{w} during each iteration is formulated as:

$$\mathbf{w}_m^{l+1} = \mathbf{w}_m^l + K \left(Y_j - \mathcal{H}[\mathbf{w}_m^l] \right) \quad (8a)$$

$$\text{with } K = PH^T \left(HPH^T + R \right)^{-1} \quad (8b)$$

where m is the sample index. As the observation operator \mathcal{H} is nonlinear, the computation of the Kalman gain matrix K utilizes the linear observation operator H estimated from the ensemble of the predicted observed quantities. By employing a matrix identity, the Kalman gain matrix K can also be formulated as [32]

$$K = \left(P^{-1} + H^T R^{-1} H \right)^{-1} H^T R^{-1}$$

where, it can be shown that the Kalman gain matrix K effectively provides an approximation to the product of the inverse of the local Hessian Matrix and the local gradient. Hence, for updating the parameters \mathbf{w} (Eq. 8a), the term $K(Y_j - \mathcal{H}[\mathbf{w}_m^t])$ implicitly utilizes the information of approximated gradient and Hessian matrices of the cost function with respect to the parameters \mathbf{w} . For a detailed derivation of the relation between the approximated derivatives of the cost function and the Kalman gain matrix, we recommend referring to Ref. [22].

The schematic of the training framework for the current application of hypersonic flows is depicted in Fig. 1. Traditional initialization of the NN parameters \mathbf{w} can lead to the prediction of non-physical values for the closure variables, which in turn can cause the flow solver to diverge. Therefore, the NN parameters are pre-trained using the output values of the baseline model, specifically $g^{(1)} = -0.09$ and $Pr_t = 1.0$. Consequently, in the first iteration, samples of the parameters are drawn around the pre-trained parameters, resulting in predicted closure variables that closely resemble those of the baseline model. Furthermore, for the first iteration, input features based on scalar invariant θ are extracted from the baseline flow field. The iterative training process, as illustrated in Fig. 1, can be summarized in the following steps:

- (a) *Ensemble generation*: Samples of NN parameters \mathbf{w} are generated based on a prescribed normal distribution. Scalar invariants θ are extracted from the predicted flow field of the previous iteration. Using each sample \mathbf{w}_m , the scalar invariants θ are then mapped to closure variables ($g^{(1)}$ and Pr_t). Each sample \mathbf{w}_m represents a different turbulence closure model, resulting in an ensemble of predicted Reynolds stress and turbulent heat flux fields.
- (b) *Forward propagation*: RANS equations are solved using each of the predicted Reynolds stress and turbulent heat flux fields. During post-processing, mean flow quantities (e.g., velocity and temperature) are extracted for each sample in the ensemble of RANS simulation results.
- (c) *Updating parameters*: Using the predicted quantities in observation space and the observation data from DNS, updated parameters \mathbf{w} are statistically inferred based on Eq. 8.

The DAFI code [33] is employed to implement the ensemble-based training. The NN-based closure model is represented by a fully connected neural network with 10 hidden layers, each consisting of 10 neurons. The rectified linear unit (ReLU) activation function is used to introduce non-linearity in the hidden layers, while linear activation is applied to the output layer. RANS simulations are performed using OpenFOAM, an open-source CFD tool based on the finite volume method. The simulations utilize the built-in explicit density-based compressible flow solver *rhoCentralFoam*, which incorporates the second order central-upwind flux scheme proposed by Kurganov and Tadmor [34]. Second order schemes are used to approximate the gradient, divergence and Laplacian terms, and the van Leer limiter is used to approximate the solution variables at cell faces. All simulations are conducted with double precision.

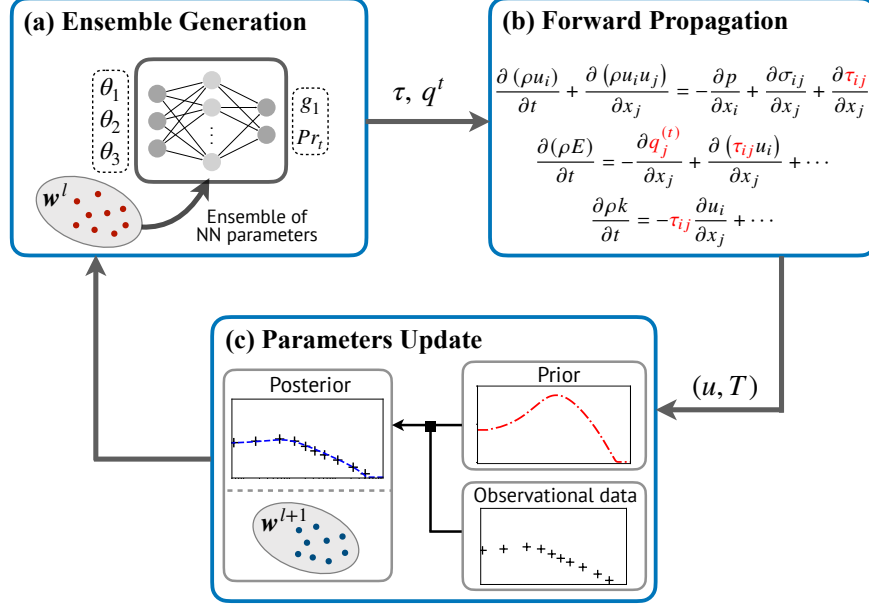


Fig. 1 Schematic of training NN-based turbulence model using ensemble Kalman method.

III. Hypersonic Flow Cases

The NN-based turbulence modeling approach has been analyzed using a DNS database from recently conducted hypersonic flow simulations [7, 8]. The simulations correspond to zero-pressure gradient flat plate turbulent boundary layer flows under cold-wall and near adiabatic conditions. These benchmark flow cases are summarized in Table 1, where freestream conditions and wall temperature for each case are provided. The listed cases cover a wide range of freestream Mach numbers and wall-to-recovery temperature ratios. All the flow cases fall within the perfect gas regime. The working fluid is air, except for the case M8Tw048, in which the working fluid is nitrogen.

Table 1 Freestream conditions and wall temperatures for hypersonic flow cases in the DNS database

Case	M_∞	$U_\infty, \text{m/s}$	$\rho_\infty, \text{kg/m}^3$	T_∞, K	T_w, K	T_w/T_r	δ_i, mm	$(x_a - x_i)/\delta_i$
M6Tw025	5.84	869.1	0.044	55.2	97.5	0.25	1.3	88.6
M6Tw076	5.86	870.1	0.043	55.0	300.0	0.76	13.8	54.1
M8Tw048	7.87	1155.1	0.026	51.8	298.0	0.48	20.0	56.9
M11Tw020	10.90	1778.4	0.103	66.5	300.0	0.20	3.7	95.0
M14Tw018	13.64	1882.2	0.017	47.4	300.0	0.18	18.8	199.3

For each case, a rectangular domain grid is used, with a relatively shorter region upstream of the flat plate where a symmetry boundary condition is applied at $y = 0$. The M6Tw076 grid is shown in Fig. 2 as an example to illustrate the specified boundary conditions. The domain size in the wall-normal direction is set to ensure that the leading edge shock wave does not interact with the top boundary. In the streamwise direction, the flat plate is extended appropriately downstream of the sampling location.

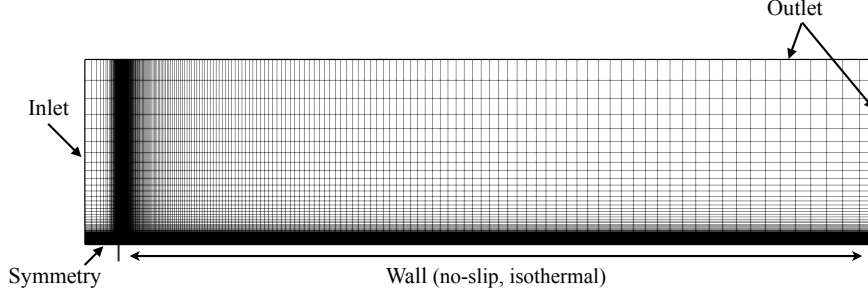


Fig. 2 Computational grid for the flat plate, with specified boundary conditions illustrated.

The sampling location (x_a) corresponds to the streamwise location along the flat plate where wall-normal profiles are provided in the DNS database. From the RANS simulation results of each case, x_a is determined by first locating the position x_i along the flat plate where the boundary layer thickness equals the inflow boundary layer thickness δ_i of the DNS data. Then, the sampling location x_a is determined using the values of $(x_a - x_i) / \delta_i$ as specified in Table 1. A similar method for determining the sampling locations has also been employed in Ref. [9] to compare RANS simulation results with the DNS database. The Reynolds number based on friction velocity and wall viscosity (Re_τ) has also been used in Ref. [6] to determine the sampling location for comparing RANS simulation results with DNS data. However, since Re_τ itself depends on the turbulence model, which is modified in each training iteration, we consider the sampling location with respect to the streamwise location x_a here. Further investigation in this regard will be conducted in future work.

For each case, four levels of grids (ultra-fine, fine, medium, and coarse) are generated by systematically refining the meshes with a refinement factor of 2. The details of the medium-level grid for each case are provided in Table 2.

Table 2 Domain size and resolution of the medium level grid for RANS simulations. Δy_a^+ refers to the y^+ height of the first cell off the wall at the sampling location.

Case	$L_x \times L_y$, m	x -range, m	$N_x \times N_y$	Δy_a^+
M6Tw025	0.27×0.10	$(-0.04, 0.23)$	250×250	0.3
M6Tw076	2.35×0.55	$(-0.10, 2.25)$	520×300	0.3
M8Tw048	3.43×0.80	$(-0.10, 3.33)$	370×260	0.3
M11Tw020	1.55×0.10	$(-0.05, 1.50)$	760×400	0.3
M14Tw018	5.60×0.70	$(-0.10, 5.50)$	520×350	0.3

To assess the adequacy of the given RANS simulation results for their intended use, the numerical uncertainty associated with the discretization error at each mesh level is calculated. The discretization error depends on the chosen grid resolution, grid quality, and the numerical scheme [35]. To evaluate the discretization error, the exact solution is approximated based on the results of the *two finest grids* using the Richardson extrapolation (RE) method [36, 37]. The

generalised form of RE is given by:

$$f_{\text{RE}} = f_1 + \frac{f_1 - f_2}{r^p - 1} \quad (9)$$

where f is a generic solution variable considered as the quantity of interest. Among the two finest grids, f_1 corresponds to the finer one. r represents the refinement factor of the grid, which is 2.0 in this work. p represents the formal order of accuracy of the numerical schemes employed. Although second-order numerical schemes are used for simulations, it is not clear if the formal order of accuracy for this problem should be 1.0 or 2.0, as the flow contains a non-grid-aligned shock wave [38]. Hence, we adopt the conservative value of $p = 1.0$.

In each case, the wall heat flux (q_w) at the sampling location (x_a) is considered as the quantity of interest. The discretization error ($\bar{\epsilon}_h$) is evaluated by calculating the difference between the estimated exact solution (f_{RE}) and the RANS solution. This error estimate is then converted to numerical uncertainty by considering the magnitude of the error estimate, along with an additional factor of safety (F_s), as follows:

$$\text{Numerical Uncertainty} = F_s |\bar{\epsilon}_h| \quad (10)$$

A factor of safety (F_s) of 3.0 is considered since the computed numerical solutions at different grid levels don't suggest to be in the asymptotic grid convergence range. The asymptotic range pertains to the range of discretization sizes where the lowest-order terms in the truncation error dominate. It is numerically established by checking whether the observed order of accuracy from numerical solutions of at least three grid levels matches the formal order. [37].

Numerical uncertainties, expressed as percentages of the estimated exact solutions, are presented in Table 3 for the three coarsest grids of each flow case. The large jump between the numerical uncertainty values of coarse and medium grid levels can possibly be due to a large difference in laminar to turbulent transition locations. Further investigation is required to eliminate these disparities, potentially by tweaking the freestream turbulence quantities. The provided values suggest that the medium grid for each case offers a reasonable trade-off between the reliability and computational efficiency of the RANS simulations.

Table 3 Numerical uncertainties for systematically refined meshes of each flow case, determined based on discretization error estimate and a factor of safety.

Case	Coarse	Medium	Fine
M6Tw025	17.96%	1.69%	1.01%
M6Tw076	43.18%	0.43%	0.67%
M8Tw048	23.07%	1.13%	1.87%
M11Tw020	13.79%	0.39%	0.20%
M14Tw018	20.50%	4.91%	2.57%

IV. Results

The ensemble-based training framework, which aims to learn a data-driven turbulence model for hypersonic flows, has been analyzed using two training setups:

- 1) *Single training case*: Observation data from one flow case M6Tw025 are used for training
- 2) *Joint training case*: Observation data from two flow cases, M6Tw076 and M14Tw018, are simultaneously used for training

The trained turbulence models are subsequently tested on the remaining flow cases from Table 1 for each of the training setups. Sparse observation data points of the wall-normal profiles for streamwise velocity (u) and temperature (T) within the boundary layer region at the sampling location are used for training. Observation data points outside the boundary layer region are excluded manually in this work, however this could be automated using the available turbulence functions that identify the boundary region (e.g. from Menter's SST model). The sparse observation points are extracted from the DNS database, with a higher concentration of points closer to the wall. This is achieved by systematically skipping an increasing number of points in the DNS database as we move away from the wall. This choice of sampling points avoids a high clustering of points towards the edge of the BL and results in roughly evenly spaced data locations when y^+ is plotted on a log scale. Moreover, during training, near-wall data points are weighted higher to place greater emphasis on improving the primary quantities of interest, i.e., wall heat flux and skin friction. This higher weighting is implemented by scaling the diagonal elements of the observation error covariance matrix R using factors within the range of $[1, 0.1]$. Here, 0.1 corresponds to the points at the boundary layer edge, and 1.0 corresponds to points at the wall.

The input features for the neural network consist of the scalar invariants θ as defined in Eq. 4. The conventional approach of scaling the input features using global minimum and maximum values often leads to skewed distributions of the input features [22], particularly in high-speed flows which involve shock waves or flow singularities. To address this issue, we employ local normalization to scale the input features. In this method, the local quantity of turbulence time scale t_s is used, and the strain rate and rotation rate tensors are normalized as follows:

$$\hat{\mathbf{S}} = \frac{\mathbf{S}}{\|\mathbf{S}\| + 1/t_s} \quad \text{and} \quad \hat{\mathbf{\Omega}} = \frac{\mathbf{\Omega}}{\|\mathbf{\Omega}\| + 1/t_s} \quad (11)$$

The scalar invariants θ are subsequently computed using these normalized strain rate and rotation rate tensors. The resulting input features fall within the range of $[-1, 1]$, avoid skewed distributions and improve the convergence behavior during training [14, 39].

With these settings in place, the turbulence model training is conducted using two different training setups. For each of these training setups, the results for the respective training and test cases are compared with the DNS database based on flow quantities, including velocity and temperature, as well as wall heat transfer and skin friction coefficients. The

heat transfer coefficient is defined in two forms, and the appropriate choice between these two forms depends on T_w/T_r . For calorically perfect gases, the *adiabatic wall* and *edge* heat transfer coefficients are given as

$$C_{h,aw} = \frac{q_w}{\rho_\infty c_p U_\infty (T_r - T_w)} \quad C_{h,e} = \frac{q_w}{\rho_\infty c_p U_\infty (T_{0,e} - T_w)} \quad (12)$$

where T_r is the recovery temperature at the wall and $T_{0,e}$ is the total temperature with respect to the boundary layer edge conditions. For higher T_w/T_r approaching 1, both the numerator (q_w) and the denominator ($T_r - T_w$) approaches zero. For such cases, $C_{h,e}$ provides a more appropriate form to quantify the heat transfer at the wall. Hence, among the flow cases given in Table 1, $C_{h,e}$ will be used to present results for M6Tw076 case.

A. Single Training Case

In this training scenario, the NN-based turbulence model is trained using DNS data for the M6Tw025 flow case and subsequently tested for the remaining four flow cases. The results of this training case are presented in Figure 3, which compares the simulation results obtained using the trained NN-based turbulence model with those from the baseline turbulence model ($k - \omega$). Additionally, the DNS data points used for training are displayed. The results demonstrate that the trained turbulence model predicts velocity and temperature profiles for the training flow case with improved accuracy.

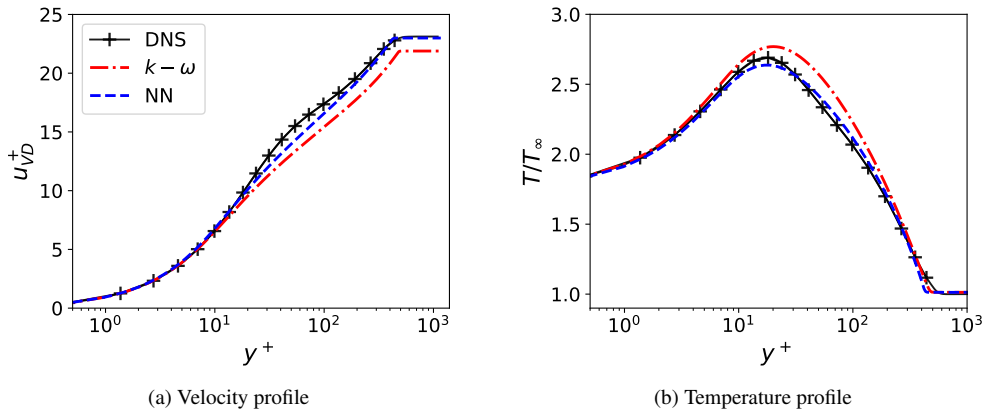


Fig. 3 Training results for M6Tw025 flow case, with sparse observation data points (+) from DNS are shown.

The wall heat transfer and skin friction coefficients, shown in Figure 4, are also predicted with significantly improved accuracy compared to the baseline model. This improvement can be attributed to the learned turbulence model that predicts the output quantities of $g^{(1)}$ and Pr_t considerably different from the baseline model, as shown in Figure 5. The predicted $g^{(1)}$ exhibits variations with respect to the input features normal to the wall within the boundary layer region, deviating from the constant value of -0.09 assumed by the baseline model. On the other hand, the predicted Pr_t remains relatively constant, albeit different from the baseline model. When compared to the variable Pr_t from the DNS

data, the predicted constant value of Pr_t appears to be roughly equal to the mean of the Pr_t profile from DNS data. The singular behavior in the Pr_t profile from DNS at $y^+ \approx 20$ (Fig. 5(a)) corresponds to the inflection in the temperature profile (Fig. 3(a)).

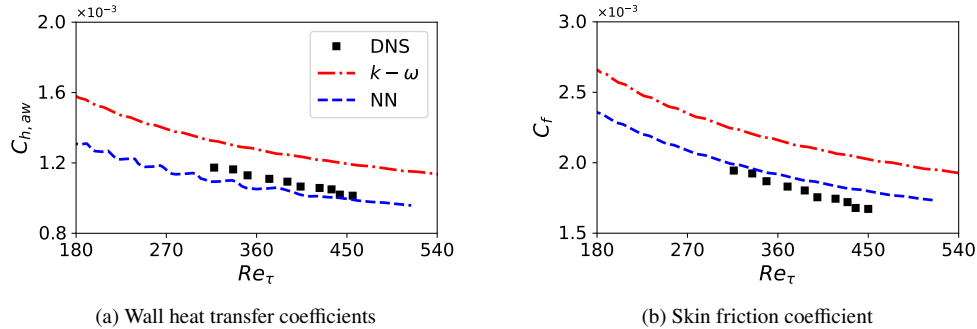


Fig. 4 Quantities of interest at the wall for the training case M6Tw025.

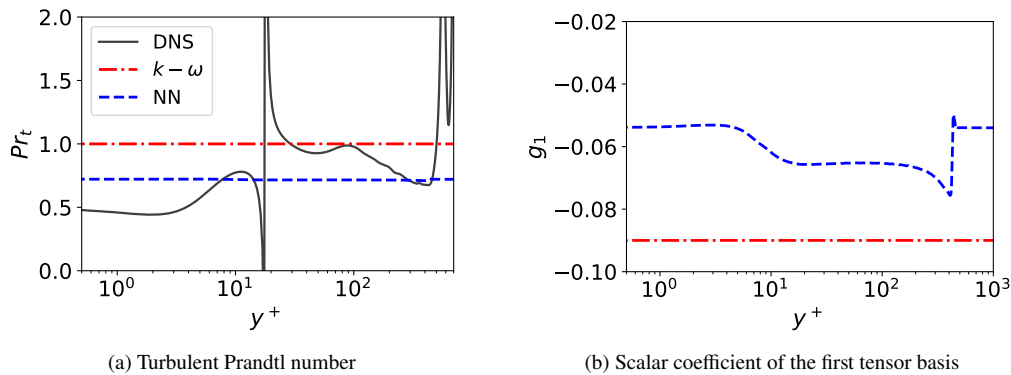


Fig. 5 Variation of learned closure variables in the boundary layer at the sampling location for the training case M6Tw025.

One prominent feature observed in the DNS data is a bump in the velocity profile (Figure 3), which the learned turbulence model is unable to accurately predict. This discrepancy is highlighted in Figure 6(a) using a grey shaded region, where the predicted velocity profile differs from the DNS training data. The inaccurate prediction appears to be caused by the lack of variation of the input features θ in that region, as also highlighted by the grey shaded region in Figure 6(b). This results in trained turbulence model predicting a uniform value of $g^{(1)}$ for that region. To address this issue, it would be necessary to introduce additional input features that can capture this variation.

The training of the NN-based turbulence model is also explored by varying the initial values of Pr_t from the previously used value of 1.0. This is accomplished by employing different values of Pr_t during the pre-training of the NN parameters and in the RANS simulation with the baseline model to extract input features for the first training iteration. Two distinct initial values of Pr_t are examined: a uniform value of 0.5 and sinusoidal variation of Pr_t in the

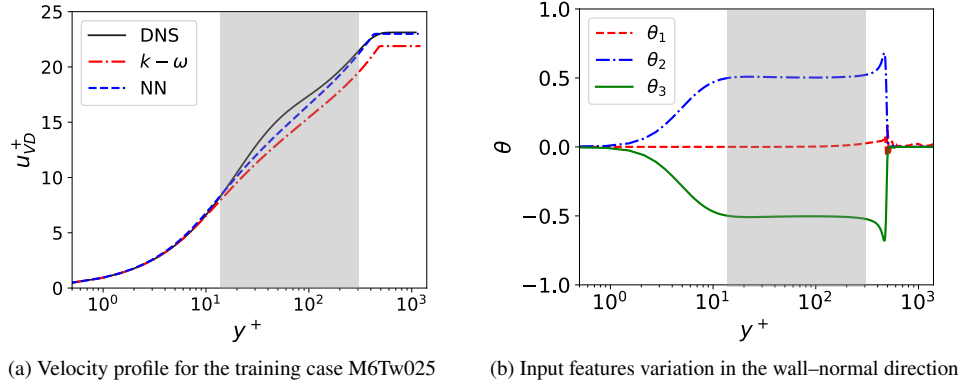


Fig. 6 For the training case M6Tw025, discrepancy of the predicted velocity profile in the shaded region is related to the lack of variation in the input features.

wall-normal direction with a mean around 1.0. The results are shown in Figure 7, where the initial and learned values of Pr_t are compared. In both cases, the predicted Pr_t by the trained turbulence model ultimately converges to the same value of Pr_t , regardless of the initial values employed for training.

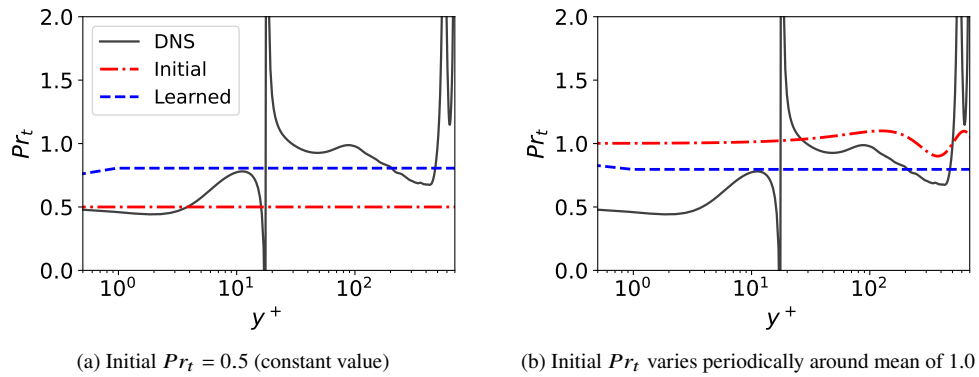


Fig. 7 Results of two different training cases with different initial values of turbulent Prandtl number (Pr_t).

The turbulence model, trained using DNS data of the M6Tw025 flow case, is tested on the remaining flow cases. Figure 8 presents the predicted velocity profiles for these test cases, showing slight improvements for all cases except for M6Tw076, for which the predictions by the trained model near the BL edge are worse than those of the baseline model. Examining the temperature profiles in Figure 9, a noticeable improvement can be observed, particularly in the peak temperatures within the boundary layer. Wall heat transfer coefficients are shown in Figure 10, where improvements can be observed for the M11Tw020 and M14Tw018 flow cases, whereas it is under-predicted for the other two test cases. Conversely, for the results of skin-friction coefficient shown in Figure 11, only slight improvement is observed for these test cases.

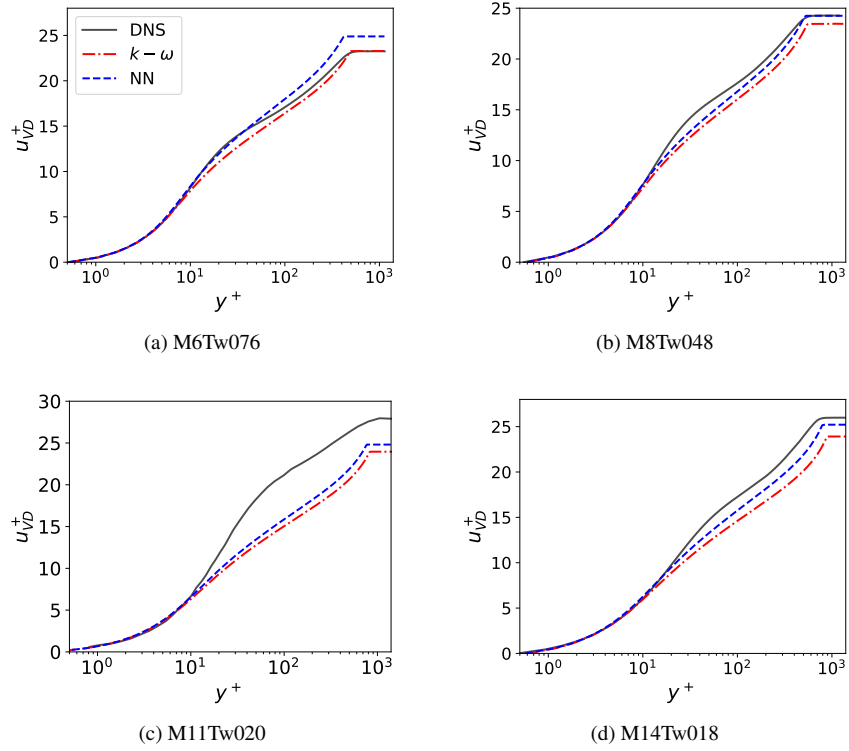


Fig. 8 Velocity profiles for the test cases, computed using the NN model trained with M6Tw025 case.

B. Joint Training Case

Here, we present the results for the joint training case, where DNS data from two flow cases are simultaneously used to train the turbulence model. In the single training case presented above, predictions for the test flow cases showed sporadic improvements. Particularly, for the flow case M6Tw076 with a relatively higher T_w/T_r , the prediction of velocity profile and wall heat transfer coefficient was significantly worse than the baseline model. Furthermore, only small improvements were observed for higher Mach number flow cases (M11Tw020 and M14Tw018). Therefore, a joint training case is considered here, where DNS data from two flow cases, namely M6Tw076 and M14Tw018, are used for training. The choice of these two flow cases for training is made in order to provide observational data from two extremes of Mach numbers, as well as wall-to-recovery temperature ratios among the available list of flow cases. A similar number of observation points from both flow cases, with a similar distribution throughout the BL, are used for joint training.

Results of the two training flow cases are shown in Figure 12, where the velocity and temperature profiles computed using the trained turbulence model are plotted against those obtained with the baseline turbulence model ($k-\omega$). Training data points from DNS of the respective flow cases are also displayed. For the M14Tw018 flow case, the trained turbulence model is able to predict velocity and temperature profiles with significantly improved accuracy. However, for the M6Tw076 flow case, the prediction of the velocity profile is worse than that of the baseline model ($k-\omega$). Since

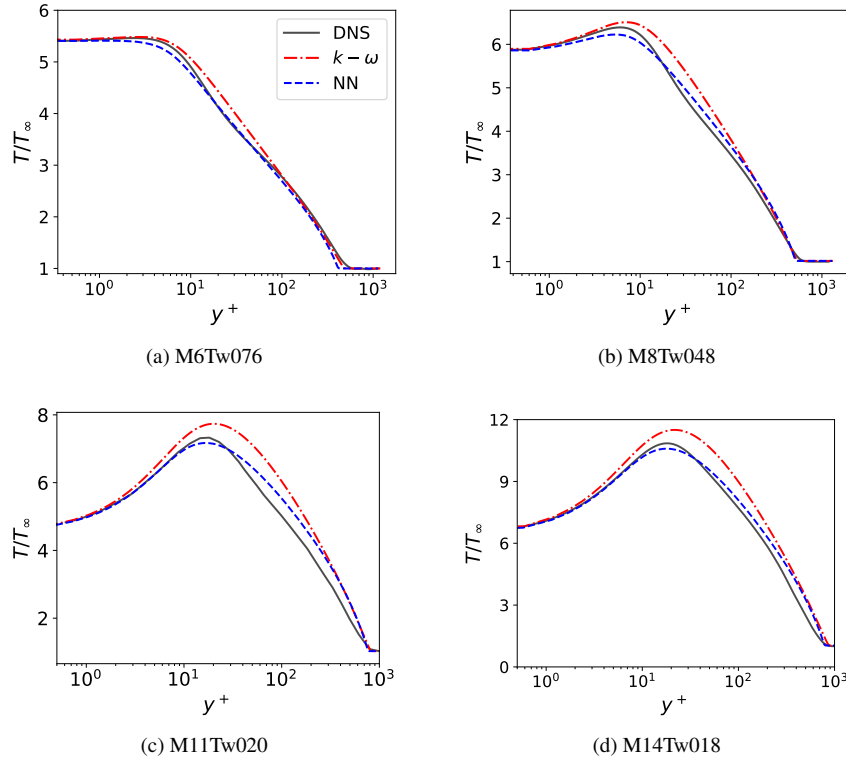


Fig. 9 Temperature profiles for the test cases, computed using the NN model trained with M6Tw025 case.

the baseline model can reasonably predict the velocity profile of the M6Tw076 flow case, it can be deduced that the standard value of $g_1 = -0.09$ performs well for T_w/T_r relatively closer to 1. As the T_w/T_r decreases, such as in the case of M6Tw025 or M14Tw018, a better agreement of the velocity profile with the DNS data requires a higher value of g_1 than -0.09 .

To further verify this observation, single training cases are also conducted separately for both M6Tw076 and M14Tw018. In both cases, the velocity profiles predicted by their respective trained turbulence models exhibit good agreement with the DNS data. However, in these single training cases, the learned values of g_1 are significantly different, with it being closer to -0.09 for M6Tw076, while it is closer to -0.05 for M14Tw018. Additionally, a test flow case M5Tw091 with higher T_w/T_r of 0.91 is also considered. Results for this test flow case, as presented in Appendix A, further emphasize that as T_w/T_r gets closer to 1, a g_1 value around -0.09 is observed as more appropriate for better predictions of mean flow quantities.

From the results of the joint training case shown in Figure 12, it can be inferred that the joint training is unable to learn the distinction of appropriate g_1 values for each flow case. This analysis is further illustrated in Fig. 13. It can be observed in Fig. 13(a) that the predicted g_1 values for both flow cases are closer to the appropriate range for the M14Tw018 flow case. Consequently, the velocity profile prediction improves for M14Tw018, but deteriorates for M6Tw076. As there is a higher discrepancy between the velocity and temperature profiles obtained from the baseline

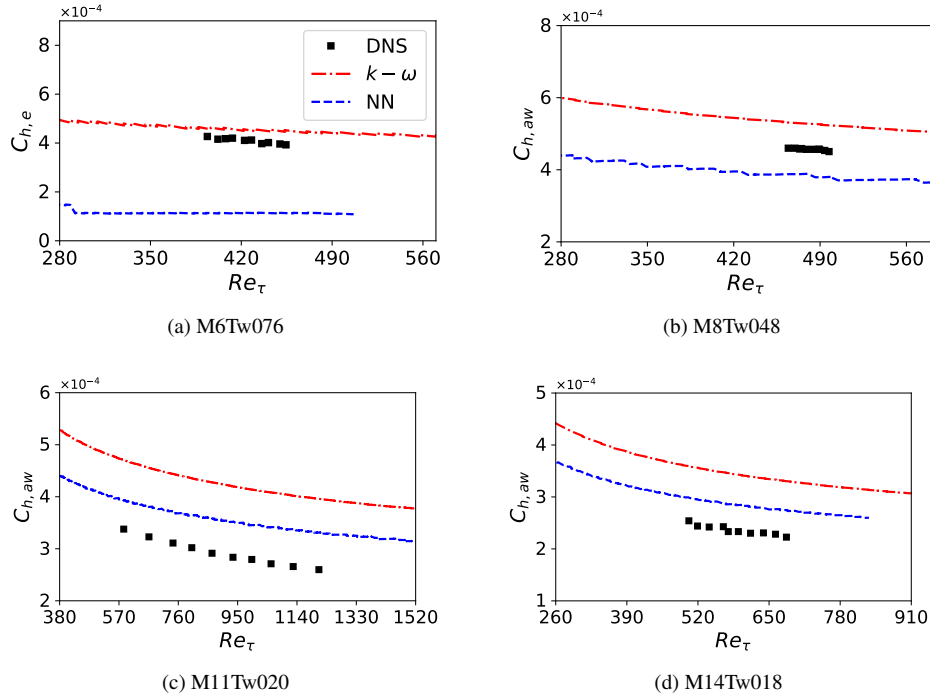


Fig. 10 Heat transfer coefficient at the wall for the test cases, computed using the NN model trained with M6Tw025 case.

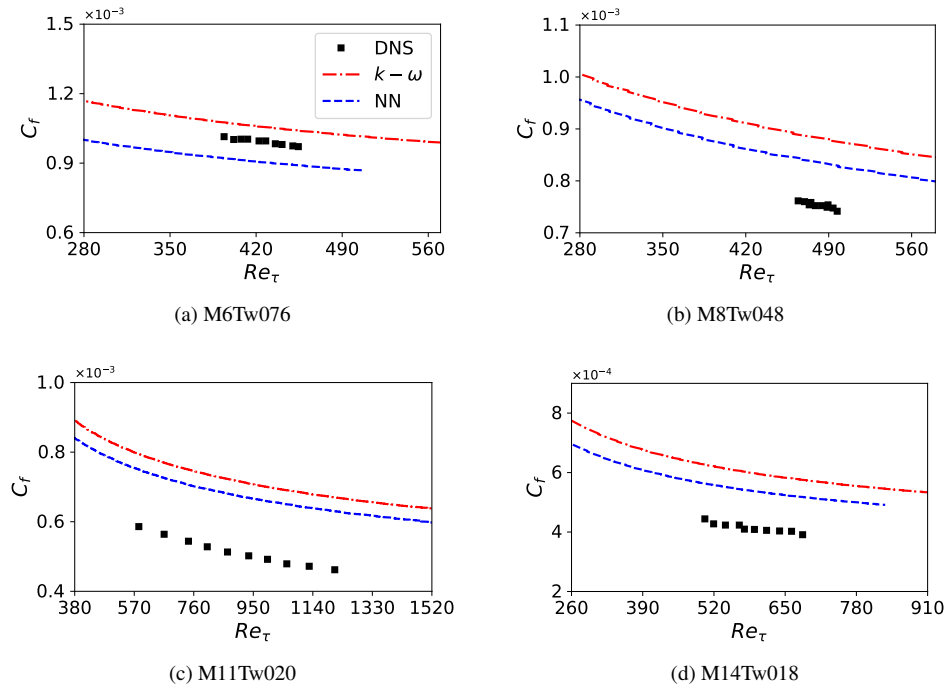


Fig. 11 Skin friction coefficient for the test cases, computed using the NN model trained with M6Tw025 case.

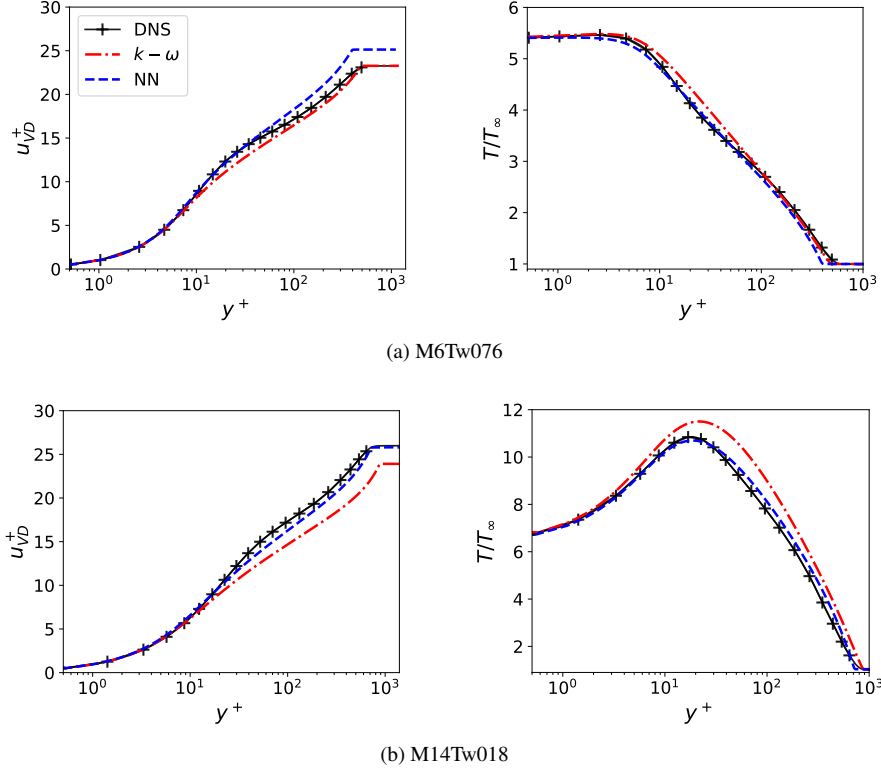


Fig. 12 Joint training results where DNS data of two flow cases is simultaneously used for training. DNS data points (+) of velocity and temperature used for training for both cases are shown as well.

model and the DNS data points of M14Tw018, the joint training is predominantly influenced by the training data of M14Tw018. Similarly, in Fig. 13(b), the predicted Pr_t values are shown to be the same for both flow cases, unlike the DNS data which indicates a difference in Pr_t profiles, particularly near the wall. This lack of distinction in the predicted quantities for the two flow cases can be attributed to the similarity in the input features, as depicted in Fig. 13(c). It can be observed that the input features for both flow cases exhibit similar variations in the wall-normal direction, and the absolute values of θ_1 , θ_2 , and θ_3 fall within the same range. This similarity in input features does not provide any basis for the neural network to learn the distinction between the two flow cases.

The wall heat transfer and skin friction coefficients for both training cases are presented in Figure 14. While improved accuracy is achieved for the M14Tw018 case, the wall heat transfer coefficient (C_h) for M6Tw076 is significantly worse compared to the DNS data. This poor performance for M6Tw076 can be attributed to the inadequate prediction of both output quantities, g_1 and Pr_t , both of which have an impact on the computation of the wall heat flux (Eq. 6). In particular, for Pr_t , it can be observed in Figure 13(b) that a significant discrepancy exists between the predicted values and the DNS data near the wall. A nonlinear variation in the predicted Pr_t is desired to better capture the variations near the wall as well as in the rest of the boundary layer region.

The jointly trained turbulence model is tested for the remaining three flow cases. Significant improvements can

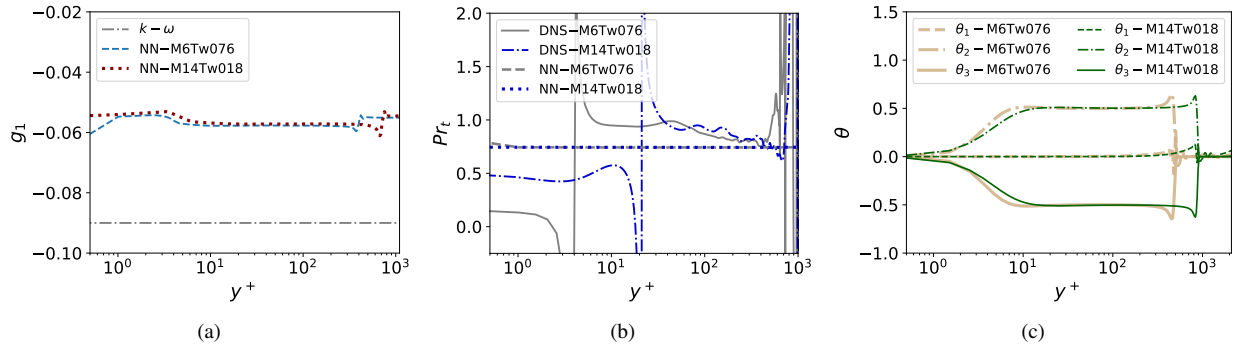


Fig. 13 Predicted output quantities (Pr_t and g_1) and the corresponding input features (θ) for M6Tw076 and M14Tw018 flow cases at their respective sampling locations.

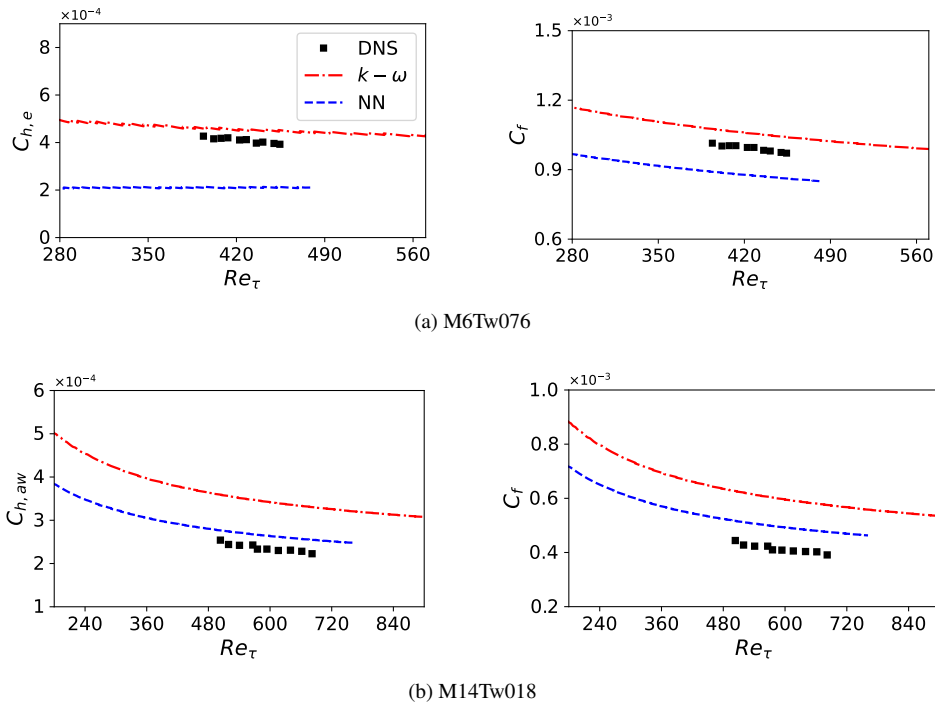


Fig. 14 Heat transfer and skin friction coefficients at the wall for the joint training cases.

be observed for all of the test cases in terms of velocity profiles, as shown in Figure 15, and temperature profiles, as shown in Figure 16. Similarly, for the wall heat transfer coefficient (C_h) and skin friction coefficient (C_f) presented in Figures 17 and 18, respectively, relatively better results are obtained in this joint training case compared to the single training case discussed earlier.

C. Discussion

The results presented above demonstrate the ability of learning an NN-based turbulence model using sparse observation data of mean flow quantities. The trained turbulence models resulted in significantly improved accuracy

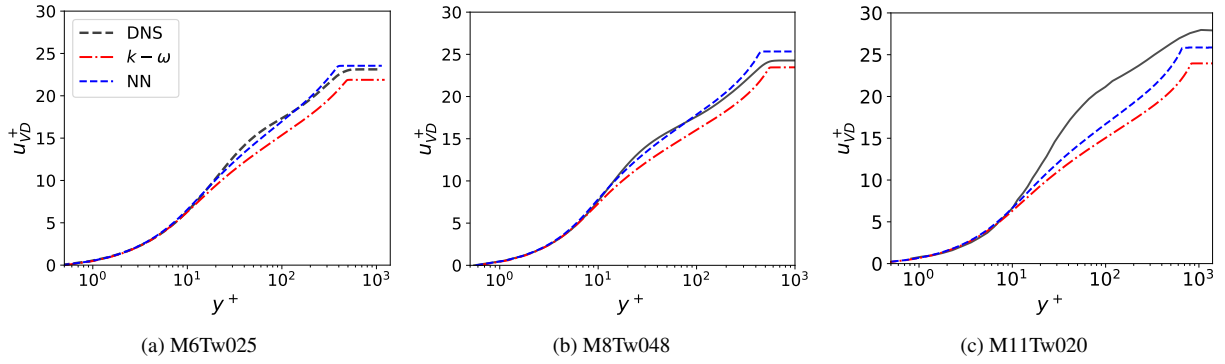


Fig. 15 Velocity profiles for the test cases, with NN model jointly trained with M6Tw076 and M14Tw018 data

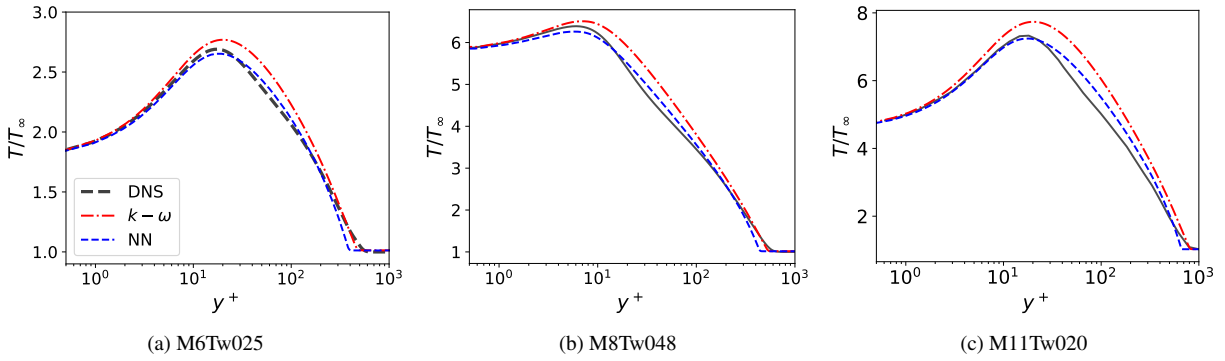


Fig. 16 Temperature profiles for the test cases, with NN model jointly trained with M6Tw076 and M14Tw018 data

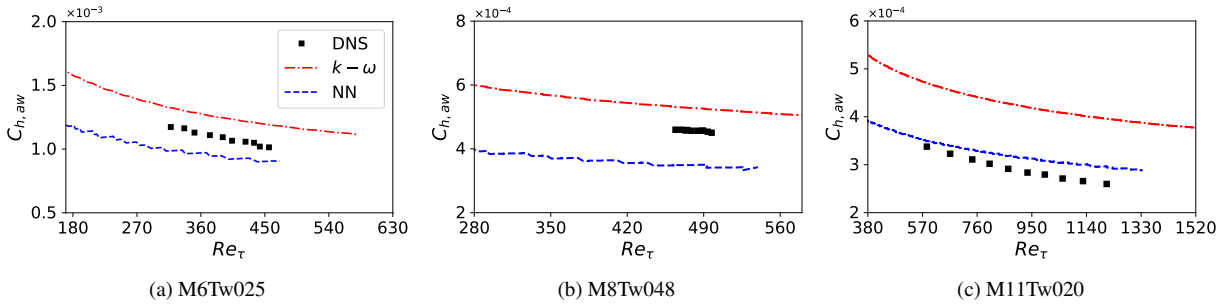


Fig. 17 Heat transfer coefficient at the wall for the test cases, with NN model jointly trained with M6Tw076 and M14Tw018 data

when computing mean flow quantities and wall heat flux. This can be compared with the recently proposed compressibility correction [9] for cold-wall conditions, where little to no improvement was observed in the computation of the mean temperature field while some improvement was observed for velocity field. However, the generalization of the trained turbulence model to test flow cases with different Mach numbers and wall-to-recovery temperature ratios does not *consistently* lead to improvements in the computation of mean flow quantities.

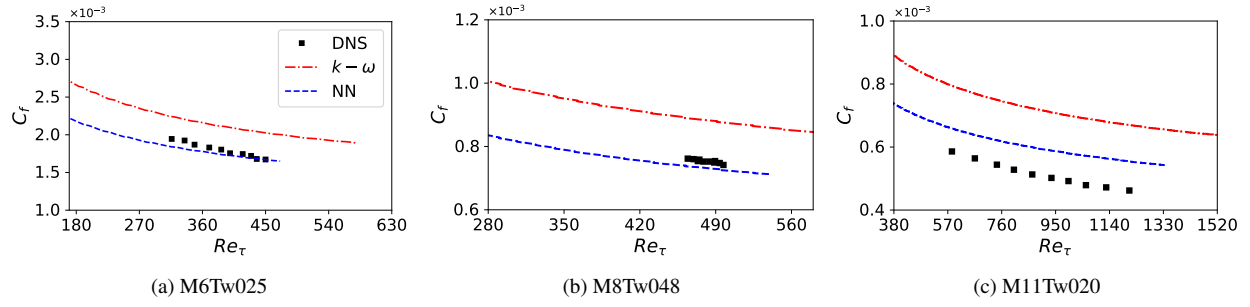


Fig. 18 Skin friction coefficient for the test cases, with NN model jointly trained with M6Tw076 and M14Tw018 data

Overall, the results highlight the need for more distinguishing information in the input features, along with the scalar invariants θ . Specifically, the input features should provide a basis for distinguishing between appropriate output quantities (g_1 and Pr_t) for different T_w/T_r . It has been illustrated in the results of the joint training case (§IV.B) and the test flow case M5Tw091 (in Appendix A) that the NN-model is unable to learn appropriate g_1 values for different flow cases. Furthermore, for Pr_t , the DNS data in Fig. 19 show a nonlinear variation in the wall-normal direction, in contrast to the constant value of Pr_t predicted by the trained turbulence models. It can be observed that near-wall Pr_t is a function of T_w/T_r , i.e. Pr_t decreases below 0.5 as the ratio T_w/T_r increases.

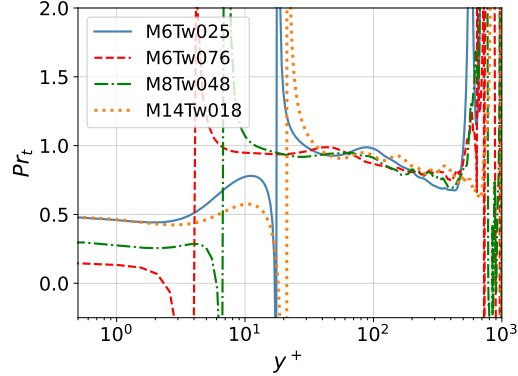


Fig. 19 Turbulent Prandtl number profiles from DNS database of different flow cases.

In general, the variation of both output quantities (g_1 and Pr_t) with respect to different flow conditions is of great importance, and such variations could potentially be learned by introducing other flow parameters as input features. In literature, scalar invariants based on temperature gradients have been used to develop heat flux closures for incompressible flows [23, 40]. Specifically for compressible wall-bounded turbulent flows with non-zero wall heat flux, a generalized Reynolds analogy (GRA) has been proposed by introducing a general recovery factor [41]. The GRA relationship between kinetic and thermal quantities has shown good agreement with the DNS data. The general recovery factor introduced in GRA accounts for the effects of wall temperature, adiabatic recovery factor, pressure

gradient, etc. Inclusion of any such additional parameters as input features needs to be considered, while preserving the embedded Galilean invariance property of the tensor basis neural networks [26]. Furthermore, the consideration of more terms from the tensor basis representation to have a nonlinear closure for the Reynolds stress tensor may provide some improvements. Future research will explore these potential avenues.

For flow cases with T_w/T_r approaching 1, the predicted temperature profiles are as accurate as those of the remaining flow cases, particularly near the wall. However, the $C_{h,e}$ predictions for M6Tw076 (Fig.10a and 14a) and M5Tw091 (Fig.20c) do not exhibit similar conformity with the DNS data. This discrepancy can be attributed to the relatively small wall heat flux values in such cases, where $C_{h,e}$ shows high sensitivity to small variations in temperature profiles, and numerical errors are likely to be large. This sensitivity is also evident in the Reynolds analogy factor (R_{af}) values for the corresponding DNS data, as highlighted in Appendix B. Despite scaling the heat transfer coefficient with respect to boundary layer edge conditions, this discrepancy persists for flow cases with relatively higher T_w/T_r values. Consequently, a different scaling should be formulated, distinct from those presented in Eq. 12.

The training cost with the ensemble Kalman method is directly related to the computational cost of the RANS simulation for the specific hypersonic flow case. Since the forward propagation of the ensemble is performed in parallel during each training iteration, the training cost can vary significantly with respect to the flow conditions, size of the computational grid, and the resources available for parallel computation. In comparison, the cost associated with the analysis and parameter updates during each iteration is negligible. Since the baseline solution serves as the starting point for training, performing forward propagation for a fraction (approximately 20%) of the total simulation time required for the convergence of the baseline solution is sufficient during each iteration. The training costs for both single and joint training cases are summarized in Table 4, which indicates the compute resources (in terms of processor cores) and associated wall times required to achieve convergence with the specified number of iterations. Prediction with the trained turbulence model is fairly efficient, as the baseline solution is used as the initial condition, and forward propagation is performed for a similar duration of simulation time as during training in each iteration.

Table 4 Summary of the computational cost for each of the training cases.

Training Case	Samples	Cores per sample	Iterations	Wall time
Single (§IV.A)	20	4	35	66 hrs.
Joint (§IV.B)	40	8	18	139 hrs.

V. Conclusion

This work presents data-driven turbulence modeling for hypersonic flows with cold-wall conditions. The turbulence model is learned to provide closure for Reynolds stress and a variable turbulent Prandtl number, with an emphasis on improving the prediction of near-wall quantities of interest, i.e., wall heat flux and skin friction. The ensemble Kalman

method employed for this purpose provides an effective tool to train the turbulence model using sparse and potentially noisy observation data of mean flow quantities.

The DNS database has been used to train the turbulence model and to assess its performance on test flow cases using the trained turbulence model. The turbulence model, trained using observation data from a single flow case, effectively learned and predicted results for the training flow case. However, for the test flow cases, this trained turbulence model provided mixed results, ranging from slight improvements to predictions worse than the baseline solution. The turbulence model trained using data from two flow cases fell short of predicting both training flow cases accurately, as the training process exhibited a bias towards learning from one flow case’s data. Nevertheless, the joint training case showed better generalizability to test flow cases compared to the single training case.

The results presented in this work highlight a few limitations and key insights that could be helpful in future research. One key limitation is the lack of variation in the predicted turbulent Prandtl number in the wall–normal direction, compared to the nonlinear variation observed in the DNS data. The turbulent Prandtl number profile from DNS data shows significant variation across the inflection point of the temperature profile. Investigating the functional dependence of turbulent Prandtl number on the local temperature gradients will be a topic for future exploration.

Furthermore, clear distinction is observed between the appropriate values of closure variables with respect to the wall–to–recovery temperature ratio. However, the formulation of input features used in this work lacked an appropriate basis for the turbulence model to learn such distinctions. Lastly, a nonlinear representation of Reynolds stress can potentially provide improvements over the currently employed linear representation. Future works will focus on addressing these limitations and employing different possibilities to enhance the generalizability of the learned turbulence model.

Appendix A. Higher wall–temperature ratio case

M5Tw091 provides a challenging test case for an NN-based turbulence model trained for cold-wall conditions. Specifically, with a T_w/T_r of 0.91 and a Mach number of 4.9, it tests the extrapolating capability of the jointly trained turbulence model for M6Tw076 and M14Tw018 cases. The freestream conditions and wall temperature for the M5Tw091 case are given in Table 5.

The results are presented in Fig.20. Unlike the cold–wall cases listed in Table1, the heat flux toward the wall in this case is small, and the temperature profile is nearly flat close to the wall. Similar to the observations made for the M6Tw076 case, the baseline turbulence model ($k-\omega$) outperforms the trained NN turbulence model in computing the velocity profile toward the boundary layer edge. This re-emphasizes the point that the standard value of $g_1 = -0.09$ performs relatively better for T_w/T_r closer to 1, whereas the jointly trained NN turbulence model predicts g_1 closer to -0.06 for this test case. Furthermore, the NN turbulence model incorrectly predicts the edge heat transfer coefficient ($C_{h,e}$) as negative, effectively representing heat transfer away from the wall. This aligns with the predicted temperature

profile in Fig. 20(b), where the temperature profile near the wall predicted using the NN turbulence model has a slight negative slope, unlike those of the $k-\omega$ model and DNS.

Table 5 Freestream conditions and wall temperature for higher wall temperature ratio case

Case	M_∞	U_∞ , m/s	ρ_∞ , kg/m ³	T_∞ , K	T_w , K	T_w/T_r	δ_i , mm	$(x_a - x_i)/\delta_i$
M5Tw091	4.9	794.0	0.272	66.2	317.0	0.91	4.0	54.0

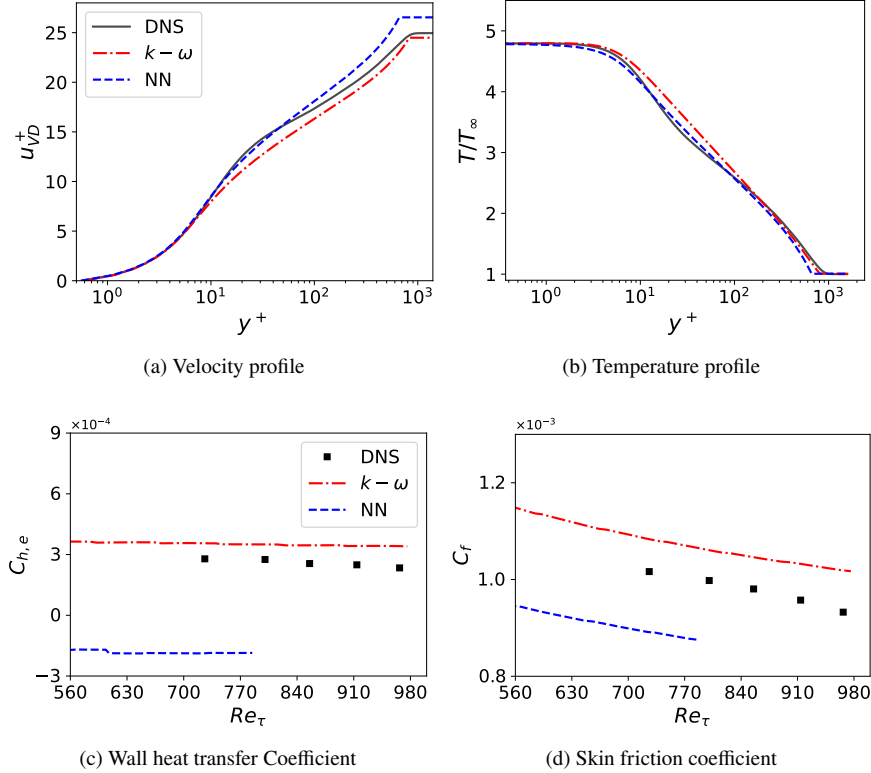


Fig. 20 Predicted results for M5Tw091 case, with NN model jointly trained with M6Tw076 and M14Tw018 data

Appendix B. Reynolds Analogy Factor for DNS data

With a known skin friction coefficient, the Reynolds analogy is often employed to predict the wall heat transfer coefficient [4]. For compressible flows, the Reynolds analogy factor is defined as $R_{af} = 2C_{h,aw}/C_f$. For the DNS data used in this work, Figure 21 shows the streamwise variation of R_{af} with respect to the Reynolds number based on friction velocity and wall viscosity (Re_τ). Across the range of Re_τ values covered by the available DNS data [42], R_{af} remains nearly constant, consistent with typical expectations, for all flow cases except M5Tw091 and M6Tw076. In these two cases, where T_w/T_r is closer to 1, mean wall heat flux values are small, resulting in relatively larger statistical errors compared to the other cases.

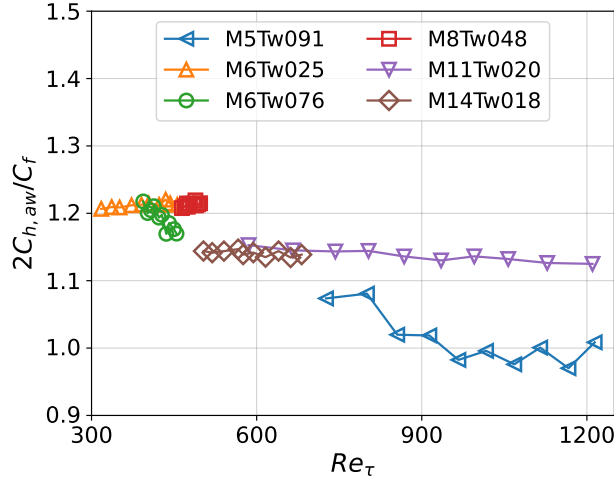


Fig. 21 Reynolds Analogy factor R_{af} for the DNS data as a function of friction Reynolds number Re_{τ} .

Funding Sources

This research was supported by the Office of Naval Research under the contract number N68335-22-C00271.

Acknowledgments

The authors would like to gratefully acknowledge Lian Duan for engaging in valuable discussions, as well as providing the DNS data. The computational resources used for this project were provided by the Advanced Research Computing (ARC) of Virginia Tech, which is also gratefully acknowledged.

References

- [1] Morkovin, M., “Effects of Compressibility on Turbulent Flows,” *Mecanique de la Turbulence*, edited by A. Favre, Gordon and Breach, New York, 1962, pp. 367–380.
- [2] So, R. M. C., Gatski, T. B., and Sommer, T. P., “Morkovin Hypothesis and the Modeling of Wall-Bounded Compressible Turbulent Flows,” *AIAA Journal*, Vol. 36, No. 9, 1998, pp. 1583–1592.
- [3] Rumsey, C. L., “Compressibility Considerations for k - ω Turbulence Models in Hypersonic Boundary-Layer Applications,” *Journal of Spacecraft and Rockets*, Vol. 47, No. 1, 2010, pp. 11–20.
- [4] Roy, C. J., and Blottner, F. G., “Review and assessment of turbulence models for hypersonic flows,” *Progress in Aerospace Sciences*, Vol. 42, No. 7, 2006, pp. 469–530.
- [5] Zhang, C., Duan, L., and Choudhari, M. M., “Effect of wall cooling on boundary-layer-induced pressure fluctuations at Mach 6,” *Journal of Fluid Mechanics*, Vol. 822, 2017, pp. 5–30.
- [6] Aiken, T. T., Boyd, I. D., Duan, L., and Huang, J., “Assessment of Reynolds Averaged Navier-Stokes Models for a Hypersonic Cold-Wall Turbulent Boundary Layer,” *AIAA SCITECH 2022 Forum*, 2022, p. 0586.

- [7] Zhang, C., Duan, L., and Choudhari, M. M., “Direct Numerical Simulation Database for Supersonic and Hypersonic Turbulent Boundary Layers,” *AIAA Journal*, Vol. 56, No. 11, 2018, pp. 4297–4311.
- [8] Huang, J., Nicholson, G. L., Duan, L., Choudhari, M. M., and Bowersox, R. D., “Simulation and Modeling of Cold-Wall Hypersonic Turbulent Boundary Layers on Flat Plate,” *AIAA Scitech 2020 Forum*, 2020, p. 0571.
- [9] Danis, M. E., and Durbin, P., “Compressibility Correction to k - ω Models for Hypersonic Turbulent Boundary Layers,” *AIAA Journal*, Vol. 60, No. 11, 2022, pp. 6225–6234.
- [10] Xiao, X., Hassan, H. A., Edwards, J. R., and Gaffney, R. L., “Role of Turbulent Prandtl Numbers on Heat Flux at Hypersonic Mach Numbers,” *AIAA Journal*, Vol. 45, No. 4, 2007, pp. 806–813.
- [11] Duraisamy, K., Iaccarino, G., and Xiao, H., “Turbulence Modeling in the Age of Data,” *Annual Review of Fluid Mechanics*, Vol. 51, No. 1, 2019, pp. 357–377.
- [12] Ling, J., Kurzwski, A., and Templeton, J., “Reynolds averaged turbulence modelling using deep neural networks with embedded invariance,” *Journal of Fluid Mechanics*, Vol. 807, 2016, pp. 155—166.
- [13] Weatheritt, J., and Sandberg, R., “A novel evolutionary algorithm applied to algebraic modifications of the RANS stress–strain relationship,” *Journal of Computational Physics*, Vol. 325, 2016, pp. 22–37.
- [14] Wu, J.-L., Xiao, H., and Paterson, E., “Physics-informed machine learning approach for augmenting turbulence models: A comprehensive framework,” *Phys. Rev. Fluids*, Vol. 3, 2018, p. 074602.
- [15] Han, J., Zhou, X.-H., and Xiao, H., “An equivariant neural operator for developing nonlocal tensorial constitutive models,” *Journal of Computational Physics*, 2023, p. 112243.
- [16] Wu, J., Xiao, H., Sun, R., and Wang, Q., “Reynolds-averaged Navier–Stokes equations with explicit data-driven Reynolds stress closure can be ill-conditioned,” *Journal of Fluid Mechanics*, Vol. 869, 2019, pp. 553–586.
- [17] Duraisamy, K., “Perspectives on machine learning-augmented Reynolds-averaged and large eddy simulation models of turbulence,” *Phys. Rev. Fluids*, Vol. 6, 2021, p. 050504.
- [18] Holland, J. R., Baeder, J. D., and Duraisamy, K., “Field Inversion and Machine Learning With Embedded Neural Networks: Physics-Consistent Neural Network Training,” *AIAA Aviation Forum*, 2019, pp. 1–20.
- [19] Michelén Ströfer, C. A., and Xiao, H., “End-to-end differentiable learning of turbulence models from indirect observations,” *Theoretical and Applied Mechanics Letters*, Vol. 11, No. 4, 2021, p. 100280.
- [20] Michelén Ströfer, C. A., Zhang, X.-L., and Xiao, H., “Ensemble gradient for learning turbulence models from indirect observations,” *Communications in Computational Physics*, Vol. 30, No. 4, 2021, pp. 1269–1289.
- [21] Ben Hassan Saïdi, I., Schmelzer, M., Cinnella, P., and Grasso, F., “CFD-driven symbolic identification of algebraic Reynolds stress models,” *Journal of Computational Physics*, Vol. 457, 2022, p. 111037.

- [22] Zhang, X.-L., Xiao, H., Luo, X., and He, G., “Ensemble Kalman method for learning turbulence models from indirect observation data,” *Journal of Fluid Mechanics*, Vol. 949, 2022, p. A26.
- [23] Lav, C., Haghiri, A., and Sandberg, R., “RANS predictions of trailing-edge slot flows using heat-flux closures developed with CFD-driven machine learning,” *Journal of the Global Power and Propulsion Society*, 2021, pp. 1–13.
- [24] Pope, S. B., “A more general effective-viscosity hypothesis,” *Journal of Fluid Mechanics*, Vol. 72, No. 2, 1975, p. 331–340.
- [25] Wilcox, D. C., *Turbulence modeling for CFD*, DCW Industries, 1993.
- [26] Ling, J., Jones, R., and Templeton, J., “Machine learning strategies for systems with invariance properties,” *Journal of Computational Physics*, Vol. 318, 2016, pp. 22–35.
- [27] Wallin, S., and Johansson, A. V., “An explicit algebraic Reynolds stress model for incompressible and compressible turbulent flows,” *Journal of Fluid Mechanics*, Vol. 403, 2000, pp. 89–132.
- [28] Boussinesq, J., “Essai sur la théorie des eaux courantes,” *Mémoires présentés par divers savants à l’Académie des Sciences*, Vol. 23 (1), 1987, pp. 1–680.
- [29] Schneider, T., Stuart, A. M., and Wu, J.-L., “Ensemble Kalman inversion for sparse learning of dynamical systems from time-averaged data,” *Journal of Computational Physics*, Vol. 470, 2022, p. 111559.
- [30] Zhang, X.-L., Xiao, H., Wu, T., and He, G., “Acoustic Inversion for Uncertainty Reduction in Reynolds-Averaged Navier–Stokes-Based Jet Noise Prediction,” *AIAA Journal*, Vol. 60, No. 4, 2022, pp. 2407–2422.
- [31] Zhou, X.-H., Wang, H., McClure, J., Chen, C., and Xiao, H., “Inference of relative permeability curves in reservoir rocks with ensemble Kalman method,” *The European Physical Journal E*, Vol. 46, No. 44, 2023.
- [32] Luo, X., “Novel iterative ensemble smoothers derived from a class of generalized cost functions,” *Computational Geosciences*, Vol. 25, 2021, pp. 1159–1189.
- [33] Michelén Ströfer, C. A., Zhang, X.-L., and Xiao, H., “DAFI: An Open-Source Framework for Ensemble-Based Data Assimilation and Field Inversion,” *Communications in Computational Physics*, Vol. 29, No. 5, 2021, pp. 1583–1622.
- [34] Kurganov, A., and Tadmor, E., “New high-resolution central schemes for nonlinear conservation laws and convection–diffusion equations,” *Journal of computational physics*, Vol. 160, No. 1, 2000, pp. 241–282.
- [35] Oberkampf, W. L., and Roy, C. J., *Verification and Validation in Scientific Computing*, Cambridge University Press, 2010.
- [36] Roache, P. J., “Perspective: A Method for Uniform Reporting of Grid Refinement Studies,” *Journal of Fluids Engineering*, Vol. 116, No. 3, 1994, pp. 405–413.
- [37] Roy, C. J., “Review of code and solution verification procedures for computational simulation,” *Journal of Computational Physics*, Vol. 205, No. 1, 2005, pp. 131–156.

- [38] Carpenter, M. H., and Casper, J. H., "Accuracy of Shock Capturing in Two Spatial Dimensions," *AIAA Journal*, Vol. 37, No. 9, 1999, pp. 1072–1079.
- [39] Liu, Y., Zhang, X.-L., and He, G., "Learning Neural-Network-Based Turbulence Models for External Transonic Flows Using Ensemble Kalman Method," *AIAA Journal*, Vol. 61, No. 8, 2023, pp. 3526–3540.
- [40] Milani, P. M., Ling, J., Saez-Mischlich, G., Bodart, J., and Eaton, J. K., "A Machine Learning Approach for Determining the Turbulent Diffusivity in Film Cooling Flows," *J. Turbomach.*, Vol. 140, No. 2, 2018, p. 021006.
- [41] Zhang, Y.-S., Bi, W.-T., Hussain, F., and She, Z.-S., "A generalized Reynolds analogy for compressible wall-bounded turbulent flows," *Journal of Fluid Mechanics*, Vol. 739, 2014, pp. 392–420.
- [42] Huang, J., Duan, L., and Choudhari, M. M., "Direct numerical simulation of hypersonic turbulent boundary layers: effect of spatial evolution and Reynolds number," *Journal of Fluid Mechanics*, Vol. 937, 2022, p. A3.